Roughening improves hydrogen embrittlement resistance of Ti-6Al-4V

Jinwoo Kim[1,†], Dylan Hall[1,2,†], Haoxue Yan[1], Yitong Shi[2], Sudha Joseph[2], Sarah Fearn[2],

Richard J. Chater[2], David Dye[2], C. Cem Tasan[1,*]

[1] Department of Materials Science and Engineering, Massachusetts Institute of Technology, Cambridge MA 02139, United States

[2] Department of Materials, Royal School of Mines, Imperial College, Prince Consort Road, London SW7 2BP, UK

Abstract

Polished surfaces of Ti-6Al-4V, the most commonly used titanium alloy, were observed to suffer from hydride growth and associated embrittlement during hydrogen charging, whereas rough surfaces suffered no such susceptibility. Direct microscopic analyses of recombined hydrogen bubbles and thermal desorption spectroscopy (TDS) revealed that the surface roughening promotes recombination of atomic hydrogen to molecular hydrogen, in turn, reducing the relative amount of atomic hydrogen uptake. Subsurface time of flight secondary-ion mass spectrometry (SIMS) further revealed that the high defect density underneath the roughened surface impedes hydrogen diffusion into the bulk. These combined effects mean that, unexpectedly, roughening significantly reduces hydrogen uptake into Ti-6Al-4V and enhances its resistance against hydrogen embrittlement – all resulting from a simple surface treatment.

Keywords

titanium; hydrogen; surface; hydrogen uptake; hydrogen embrittlement;

[†] These authors contributed equally to this work.
[*] Corresponding author.
E-mail address: tasan@mit.edu (C.C. Tasan)

1. Introduction

Titanium alloys are widely used in demanding engineering applications due to their high specific strength, corrosion resistance and excellent fatigue limit strength-to-weight ratio [1]. They have been central to the development of jet engines and airframes for the aerospace industry, emerging as the chosen materials for safety-critical components such as blades and disks, as well as airframe components subject to complex loads such as wing boxes and landing gear [1–3]. Hydrogen embrittlement (HE) has been an important concern especially in the power generation, pipeline and aerospace industries, causing catastrophic failures of high-strength components [4,5]. Due to their extensive use in engineering applications involving hydrogen, steels have received by far the most research attention of any material in this field. In contrast, prior to the 1950s, titanium was widely considered to be insusceptible to HE in aqueous environments due to its protective oxide film [2]. However, from the 1960s onward evidence accumulated that hydrogen leads to a range of degradation phenomena in titanium, which continues to cause engineering concerns for industry [2,6–10]. The majority of research in the hydrogen embrittlement (HE) of titanium focuses on the behavior of hydrogen once it is absorbed into the metal [2,8,11]. In this work we focus on the initial adsorption/absorption processes at the surface [12,13].

The surface state is a critical engineering variable controlling the absorption of H into a metal. For example, the effectiveness of surface oxide layers in limiting H-absorption led to the exploration of H-permeation barrier coatings for the prevention against HE in steels [14,15]. The presence of surface deformation or roughness can also influence H-uptake. For example, the effect of plastic deformation on electrochemical activity has been investigated for various metals in the context of corrosion [16–21] or in the field of electrochemical catalysts [22–25]. Electrons around a peak escape easier than those in a valley, thus, surface roughness increases local fluctuation of the electron work function, which leads to accelerated corrosion on a rough surface [16]. Plastic deformation, which generates an increase in surface roughness, residual stress as well as dislocation density, generally promotes the corrosion of metals, as reported for the case of copper [16,21], pipeline steel [20] and Ti-6Al-4V [17,19]. In plastically-deformed Ti-6Al-4V, both surface roughness and near-surface dislocation density influence the corrosion behavior. The

development of surface roughness plays a predominant role in the higher corrosion current density [19]. The rise in dislocation density, on the other hand, can also increase the passivation current density by multiplying the number of active dissolution sites in the passivation film [17]. These effects create significant engineering concerns, yet, decoupling their role can be challenging since they can be introduced (at varying levels) even by the application of a single surface treatment. Moreover, there are interesting opportunities that arise. For example, as will be shown in Figure 1, intriguing HE-resistance behavior can be realized even by simply cutting Ti-6Al-4V specimens. This is especially interesting since cut edges are typically detrimental to mechanical properties (e.g. cause reduction in formability of sheet metals) [26–28]. An improved understanding of this mechanical response also requires physical insights regarding the underlying microstructural processes.

With these motivations, here we examine hydrogen effects in Ti-6Al-4V. To this end, systematic electrochemical charging experiments and mechanical tests were performed, varying only the surface characteristics between tests. Clear distinctions between specimens with different roughness were observed upon electrochemical H-charging, both in the microstructure and in the resulting mechanical response during tensile tests. In order to better understand the H-transport process through the surfaces with different finishes, we carried out a quantitative microscopic analysis of hydrogen recombination, thermal desorption spectroscopy (TDS) and time-of-flight secondary ion mass spectroscopy (ToF-SIMS) measurements, and discussed these results in connection with the surface microstructure maps obtained.

2. Experimental methodology

2.1. Specimen preparation and tensile tests

A commercial Ti-6Al-4V alloy with a bimodal microstructure containing lamellar and equiaxed regions was used in this study. The alloy met the ASTM B265 specification [29] (initial H concentration < 15 wppm). The microstructure is typical of aeroengine Ti-6Al-4V disk product, with primary α grains (~20 μm in size) and transformed β regions composed

of secondary α lamellae separated by continuous β phase. A backscattered electron (BSE) micrograph of the starting material is shown in Figure 1(a), where the α phase appears dark, and the β phase appears bright. An electron backscattered diffraction (EBSD) inverse pole figure map of the same region is shown in Figure 1(b) which indicates a reasonably weak α texture with no evidence of macrozones. The secondary α lamellae occur in colonies of similar orientation and therefore can often appear as single grains in such EBSD maps.

Room temperature electrochemical H-charging experiments were carried out using an electrochemical charging setup described in a previous work [30]. Although the setup was designed primarily for *in situ* use in a scanning electron microscope (SEM), it was used outside of the SEM for this work. A plate specimen is fixed to the top of the device, sealing a chamber which contains the electrolyte and a platinum counter electrode (Figure SI1 in Supplementary Materials). In contrast to a normal electrochemical H-charging method that immerses a whole specimen into a liquid electrolyte, the setup charges hydrogen only at one flat side of a plate specimen, and the electrolyte is not in contact with any sharp edge of the specimen. A sharp edge would have an influence on H-charging similar to the roughness effect investigated in this work. By utilizing the setup, we could exclude the edge effect as well as provide uniform hydrogen flux to the charging surface.

Ti-6Al-4V plates were H-charged using a solution of 5 vol.% sulfuric acid + 5g/L ammonium thiocyanate in distilled water as the electrolyte. The setup ensures that only a circular area of 14 mm diameter is charged, allowing the nominal current density to remain constant for each specimen. A current density of 0.5 mA cm^{-2} and a charging time of 40 h were used for all specimens. Four different types of specimens were charged, and the only alteration among the specimens was the preparation method used for the specimen charging surface, which is summarized in Table 1. A larger number in the specimen name implies a finer surface finish for its final preparation step. A thickness-controllable specimen mount was used for grinding and polishing the specimens (see Supplementary Materials for the details), and the final thickness of the plate specimens was 300-400 μm with an error of ± 10 μm within a single plate (measured using a digital micrometer).

109

Table 1. Details of the methods used to prepare the H-charging surface of each specimen. Whole preparation steps of each specimen include the preparation steps of the one above it.

Specimen Name	Final preparation step	Details of final surface preparation step
S1	As-cut	Cut using wire electrical discharge machining (WEDM)
S2	Ground	Ground with 800 grit silicon carbide grinding papers (~12 µm particle size)
S3	Coarse-polished	Polished with 3 and 1 um diamond suspensions in sequence
S4	Fine-polished	Polished with a mixture of a basic colloidal silica suspension (pH 9.8, ~50 nm particle size) and 30% hydrogen peroxide by a volume ratio of 85:15.

112

Uniaxial tensile tests were performed to investigate the macroscopic HE. Tensile coupons with gauge dimensions of 3 mm length and 1 mm width were machined from the uncharged and H-charged specimens using wire electrical discharge machining (WEDM). A maximum of four tensile specimens was extracted from a single H-charged plate, each with the entire gauge section located inside the H-charged area. A Deben MTEST2000 micro-mechanical testing system was used for conducting the tensile tests at a strain rate of 5×10^{-4} s^{-1}. Digital image correlation (DIC) was used to measure the strain values using a sprayed speckle micropattern on the specimen surface.

121

2.2. Surface and sub-surface characterization

Prior to H-charging, optical analysis of the specimen surfaces was carried out using a Zygo optical microscope fitted with a scanning interferometry detector for analyzing surface topography. An area of 437.5 µm × 437.5 µm was analyzed with 1000 × 1000 pixels (data points) for each specimen. Waviness (macroroughness and inclination) was calculated by interpolation of a 10 × 10 grid in the whole range of data points for each scan, and removed from the raw data of surface topography. Surface topography images (Figure 4) and quantified values (Table 3) were obtained from the waviness-corrected data.

The specimens were characterized prior to H-charging using a JEOL JEM-2100F transmission electron microscope (TEM) at 200 kV to observe the microstructure

5

132   underneath charging surface. TEM foils were prepared by focused-ion beam (FIB) lift-out

133   with a Ga+ beam source at 30 kV in a dual beam FEI Helios Nanolab 600. A platinum

134   containing layer was initially deposited on the surface to minimize damage during ion

135   milling. The foils were thinned to become electron transparent with a thickness of ~150 nm.

136   TEM images were taken under scanning TEM (STEM) mode to obtain good microstructural

137   and dislocation contrast; complementary STEM-EDS was also performed (see

138   Supplementary Materials). Post-charging microstructural investigation was carried out

139   using a Tescan MIRA3 SEM equipped with an EDAX Hikari EBSD camera. All cross-section

140   specimens for SEM-EBSD were prepared by wet grinding with SiC paper down to 800 grit,

141   polishing with 9 μm diamond suspension, and final polishing with a neutralized colloidal

142   silica suspension (a mixture of a basic colloidal silica suspension (pH 9.8, ~50nm particle

143   size) and 30% hydrogen peroxide by a volume ratio of 85:15) to avoid hydride formation

144   during polishing.

145

2.3. Hydrogen entry investigation

147   We measured the amount of hydrogen molecules (H_2) formed by recombination of H

148   to H_2, using an electrochemical cell combined with an optical microscope (OM, Olympus BX-

149   41 metallographic microscope). The structure of the experimental setup is described in

150   Figure 7(a). The specimen was covered with a polytetrafluoroethylene (PTFE) tape with a

151   silicone-based adhesive, and only a small specimen area less than 1×1 mm^2 was exposed to

152   the electrolyte, as shown in the examples in Figure 7(b). A 6mm-tall acrylic cell body with a

153   cylindrical hole (diameter = 6.35 mm) was placed on the specimen, and the hole was filled

154   with the same electrolyte for H-charging. A Pt wire shaped into a ring was used as the counter

155   electrode and was placed at the top of the cell. A slide glass was used to cover the electrolyte

156   and to trap hydrogen bubbles inside the cell. OM images of the exposed specimen area with

157   hydrogen bubbles and the area below the slide glass were taken through the slide glass and

158   the electrolyte during H-charging with a current density of 2.5 mA cm^{-2} (most of hydrogen

159   bubbles were trapped on the PTFE surface as shown in Figure 7(b), and few bubbles were

160   observed below the slide glass.).

161   Thermal desorption spectroscopy (TDS) was conducted for H-charged specimens,
162   using a SEM-TDS setup. A general-purpose residual gas analyzer unit (MKS e-Vision 2) and a
163   heating module (Kammrath-Weiss MZ.H12) were installed in the Tescan MIRA3 SEM. 0.3
164   mm-thick specimens with different surface finishing steps were pre-charged with H for 40 h
165   with the same electrochemical cell with the bubble OM analysis (diameter of the H-charged
166   area = 6.35 mm) before the TDS measurements. The residual gas analyzer measured the H_2
167   partial pressure (P_{H2}) while the specimen was heated up to 900 ℃ with a heating rate of 10
168   K/min and cooled down to 50 ℃ by turning off the heater. The P_{H2} curve during cooling was
169   used as the background signal curve and was subtracted from the heating curve.

170   Time of flight secondary-ion mass spectrometry (ToF-SIMS) was carried out on the
171   S2 and S4 specimens after H-charging to compare H content in the near-surface region. The
172   specimens were electroplated with a 20 μm-thick Ni layer prior to analysis, as this acts to
173   protect the specimen surface during ion milling and serves as a useful interface for reference
174   to the specimen surface. The Ni plating was conducted using a Watts bath solution of $NiSO_4$
175   (0.38 M), $NiCl_2$ (0.12 M), and H_3BO_3 (0.5 M) and a current density of 10 mA cm^{-2}. A focused
176   ion beam (FIB) of Xe$^+$ ions was used to mill ramps from the surface of the two specimens in
177   a Hiden Analytical Hi5 SIMS instrument, creating a surface that allows the secondary ion
178   signal to be analyzed with depth into the specimen. The ramps have an approximate size of
179   300 μm x 60 μm at an angle of 10 degrees into the specimen. The ramps were then analyzed
180   using Bi$^+$ ions with a separate SIMS instrument (IONTOF TOF.SIMS5-Qtac100 LEIS) coupled
181   with a ToF detector.

182

183   **3. Results**

184   **3.1. Effect of surface finish on HE behavior**

185   The uniaxial tensile response for each of the H-charged specimens was investigated
186   to check the influence of H-charging. Figure 1(c) shows the stress-strain curves of the
187   different specimens after H-charging, and Table 2 summarizes the average properties based
188   on three repeats (error given by standard deviation). Interestingly, the H-charged specimens

of S1 and S2 exhibit similar tensile response to the uncharged S1 specimen, with a slight increase in fracture strain instead of the drastic reduction normally expected after H-charging [10,31]. In contrast, both polished specimens show premature fracture, with fracture strain reduced to 2.6% and 1.8% for the S3 and S4 specimens, respectively. The local strain maps captured at the moment before failure from DIC analysis (inset images in Figure 1(c)) indicate a transition from ductile to brittle failure when comparing the S2 and S4 specimens. The S2 specimen exhibits local strain over 40% at the point of failure and clear necking with strain bands visible at ~45°, which is typical of ductile failure. For the S4 specimen, the strain distribution is relatively uniform and fracture occurs without necking, which is characteristic of brittle failure. It is also observed that the average proof stress of the two polished specimens was ~100 MPa lower than the uncharged material. The decrease in yield strength is consistent with the literature [10,32,33], as hydride formation typically reduces the yield stress due to the generation of internal stresses from the volume expansion.
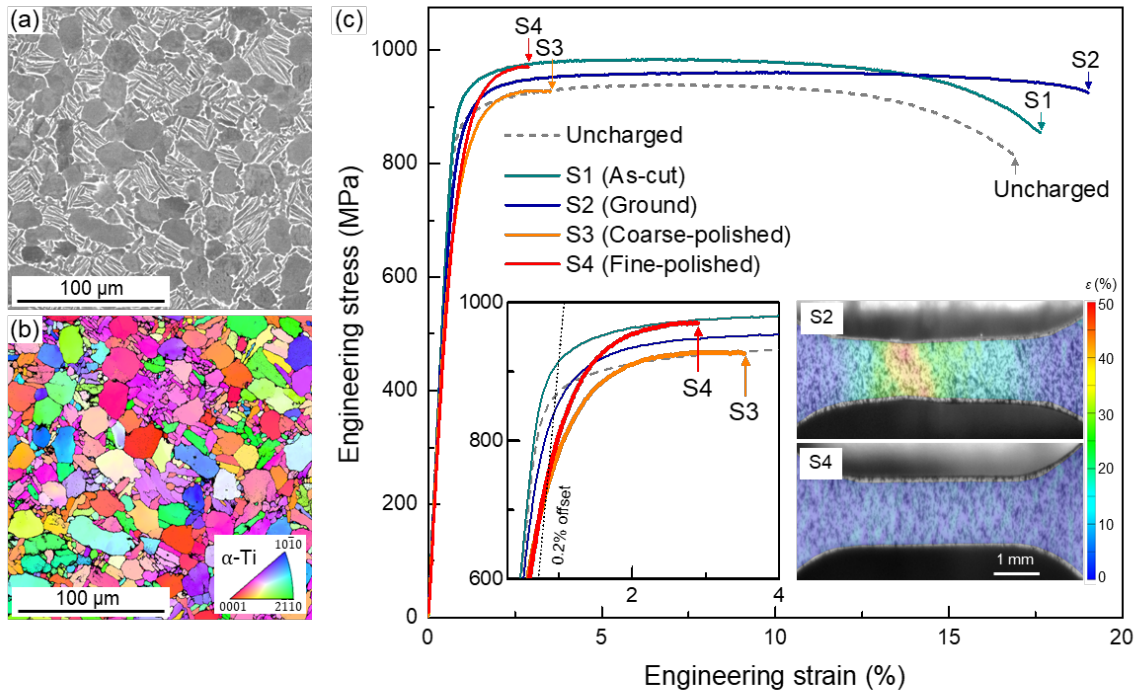
Figure 1. (a) BSE micrograph and (b) EBSD inverse pole figure map of Ti-6Al-4V alloy used in this study. (c) Tensile stress-strain curves of the uncharged specimen and H-charged specimens with four different surface states. The uncharged specimen was tested in the as-cut state. The inset graph shows an enlarged plot of stress-strain curves near fracture point of polished specimens. The inset images show the DIC maps of local Von Mises strain at the moment before failure for the ground (S2) and fine-polished (S4) specimens.

Table 2. Average mechanical properties of specimens obtained from three repeats for each case.

Specimen	0.2% proof stress (MPa)	UTS (MPa)	Fracture strain (%)
Uncharged	830 ± 20	912 ± 27	15.0 ± 1.2
S1	880 ± 19	963 ± 21	17.8 ± 1.2
S2	820 ± 15	952 ± 7	17.4 ± 2.2
S3	730 ± 8	912 ± 19	2.6 ± 0.2
S4	730 ± 40	961 ± 12	1.8 ±0.4

In the following analyses, we will focus our attention mostly on the difference in the failure strain between the non-polished (S1 and S2) and polished (S3 and S4) specimens. There are, however, as can be seen in Fig. 1 and Table 1, several other differences among the measured property values. To assess the significance of the differences, we carried out an error propagation analysis (See Supplementary Materials for the details). Miniaturizing test coupons make experiments more susceptible to influence from factors such as residual stresses, misalignment, and surface effects (particularly relevant here due to the different surface finishes used) [34]. The uniformity of specimen thickness also influences observed stress values. Although the thickness deviation of 10 μm in a single specimen is fairly high precision for manual thickness control, it causes ∼ 3 % error of stress values in a 350 μm-thick specimen. These factors create larger errors than those generated purely through measurement uncertainty, so it is not these experimental errors that the significance of the results will be measured against. In general, the variations in flow stress and UTS between specimens fall within the error range (the sum of the observed errors based on repeats and ∼ 3 % error by the non-uniformity of thickness), so little attempt is made to compare these values among specimens. However, the drastic decrease in fracture strain between polished and non-polished specimens is certainly significant, since the change is several times higher than the largest error reported. In the following sections, we focus on the origin of the different fracture strain in the H-charged specimens – in other words, the different susceptibility to hydrogen embrittlement by surface state.

Figure 2 presents the cross-section microstructures of H-charged specimens. Compared to the uncharged specimen in Figure 1(a), both polished specimens (S3 and S4) show new dark regions inside α grains as well as at the α/β phase boundary. The EBSD phase

9

map in Figure 3 indicates that the new dark phase is a hydride phase, which corresponds to a previous work [10]. Kim et al. and Chang et al. reported that the initial hydride phase in the Ti-6Al-4V alloy is formed at the α/β phase boundary (indicated by yellow arrows in Figure 2(f,h)) and has a face-centered tetragonal crystal structure of stoichiometry close to $TiH_{1.5}$, as predicted by density functional theory calculation [10,35,36]. By further H-ingress, hydride laths would grow inside the primary α grains, similar to the hydrides that form in α-Ti alloys [31,37]. The hydride phase was observed throughout the entire thickness of the H-charged S3 and S4 plates. This is in contrast to, e.g. the electrochemical charging of single phase α-Zr alloys, where a hydride layer is formed that must then be interdiffused at elevated temperatures [38]. The solubility of H in α-Ti is low at room temperature, but is much higher in β-Ti [2], and so continuous β films can permit hydrogen permeation throughout the sample, as observed here. The formation of the soft-yet-brittle hydride phase is well known to result in severe embrittlement [10], as observed in Figure 1(c). Because the hydride forms at α/β phase interface throughout the sample, rather than just the formation of a hydride rim, this leads to embittlement of the entire material. In contrast, even after H-charging for 40 h, both S1 and S2 specimens have a similar microstructure to the uncharged material, with no observed hydride formation (Figure 2(a-d)). This suggests that the absence of clear embrittlement in these two specimens originates from the reduced H-absorption, and the ground or as-cut surface finishes generate some kind of barrier to H entry and transport, which will be discussed further in the following sections.
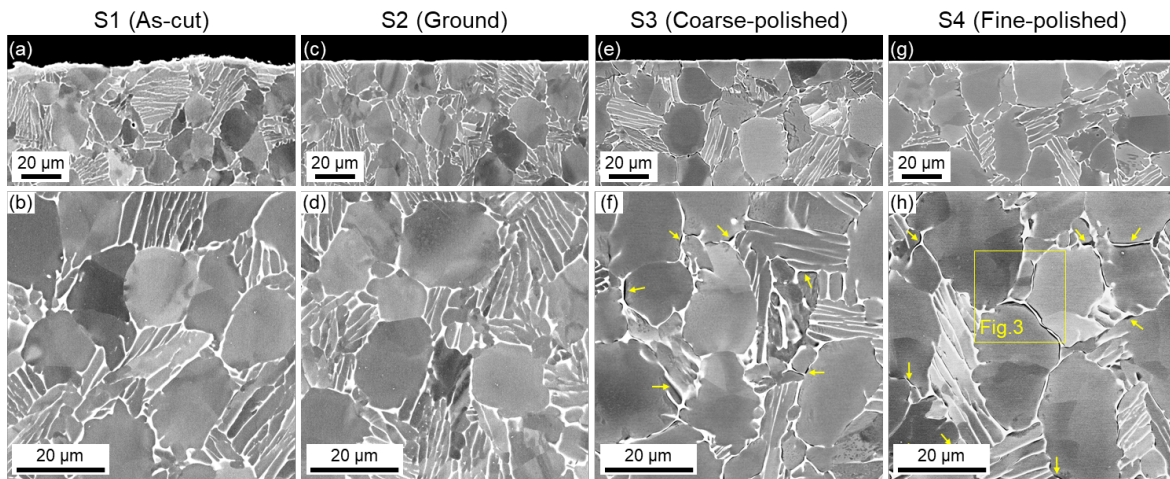
Figure 2. Cross-section BSE images of the four specimens with different surface finishes, after H-charging for 40 h. (a,b) S1, As-cut. (c,d) S2, Ground. (e,f) S3, Coarse-polished. (g,h) S4, Fine-polished. The upper row are images near the charging surfaces and the lower row are images near the center of the specimen.
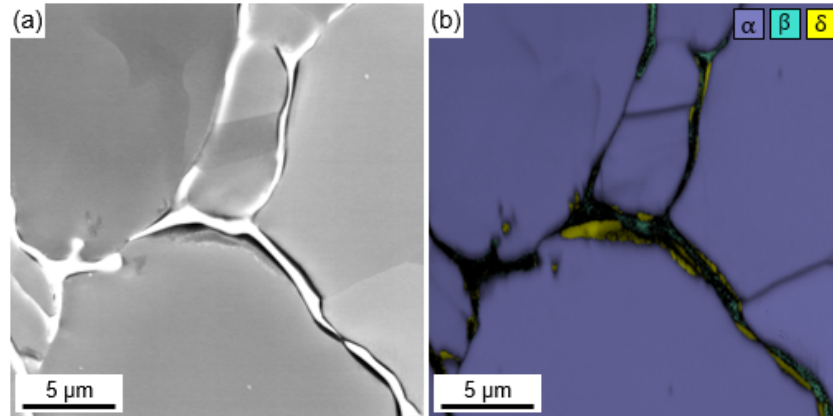
Figure 3. (a) BSE image and (b) EBSD phase map of the fine-polished (S4) specimen after H-charging for 40 h. Data points only with confidence index over 0.1 are shown here. Note that the hydride phase observed in the Ti-6Al-4V alloy has a slightly distorted structure (c/a ~ 1.013) compared to the equilibrium fcc δ-hydride phase found in pure Ti, and the β-phase is not well indexed (black) in the EBSD measurement due to non-uniform lattice expansion by H [10,39].

3.2. Surface roughness and subsurface deformation

Surface finish alters surface roughness and degree of deformation under the surface, both of which could influence H-entry and transport at the charging surface. Optical microscopy images of the four specimen surfaces before H-charging are shown in Figure 4(a-d). Both the non-polished surfaces (S1 and S2) exhibit sharp and protruding features, which are mainly re-solidified perturbations and plastically deformed clumps from grinding for the S1 specimen and S2 specimen, respectively. The S3 specimen has relatively shallow scratches but otherwise has a featureless surface, and the S4 surface is a mirror-like flat surface without any perceptible scratching.

For each area shown in Figure 4(a-d), surface topography maps were created by scanning interferometry, and the roughness and z-height distribution of each specimen was analyzed quantitatively based on the topography maps, which is shown in Figure 4(e-h). The clearly different levels of color contrast between the surface topography maps of the four specimens show the large dependence of surface fluctuation on surface finishing (note that the z-height scale in Figure 4(e) is 100X larger than the other three maps in Figure 4(f-h)). Figure 4(i) presents the line profiles of z-height values across the scan areas in the diagonal direction. In the surface profiles, the S1 and S2 specimens exhibit the fluctuation of z-height in the levels of ~20 μm and ~ 0.4 μm, respectively, while the polished specimens show

11

fluctuations of less than 0.1 μm. The surface profile of the S1 and S2 specimens tends to have more protruded peaks (local maxima) and valleys (local minima), while the polished specimens have relatively wide plateaus with dispersed valleys. It also corresponds to the probability distributions of z-height in S3 and S4 specimens, Figure 4(j), that have maximum probability points shifted to $+z$ direction from the origin.

These characteristics of surface roughness and z-height distribution could be quantified in several parameters, such as arithmetic mean roughness (R_a), root mean square roughness (R_q), skewness (Sk) and kurtosis (K) [40]. R_a is the arithmetic average of the absolute vertical deviation from the average height (m) and R_q is the standard deviation of vertical distance from the average height, both of which are widely used as standards to evaluate surface roughness.

$$R_a = \frac{1}{L_x L_y} \int_0^{L_y} \int_0^{L_x} |z(x,y) - m| dx dy \tag{2}$$

$$R_q = \sqrt{\frac{1}{L_x L_y} \int_0^{L_y} \int_0^{L_x} [z(x,y) - m]^2 dx dy} \tag{3}$$

$$m = \frac{1}{L_x L_y} \int_0^{L_y} \int_0^{L_x} z(x,y) dx dy \tag{4}$$

Sk and K are the third and fourth moments of amplitude probability function, respectively, which represent an asymmetric spread of probability distribution far from a symmetric Gaussian function as well as the distribution of peaks and valleys in a profile.

$$Sk = \frac{1}{L_x L_y \sigma^3} \int_0^{L_y} \int_0^{L_x} [z(x,y) - m]^3 dx dy \tag{5}$$

$$K = \frac{1}{L_x L_y \sigma^4} \int_0^{L_y} \int_0^{L_x} [z(x,y) - m]^4 dx dy \tag{6}$$

The values of average roughness and height descriptors (Sk and K) obtained from each topography map are listed in Table 3. The calculated surface roughness values correspond well to the qualitative insights from the surface line profiles. The variation of Sk and K values with surface finish will be discussed later in detail in the Discussion section.

During H-charging, each specimen was subjected to a constant charging current,

fixing the nominal current density. However, the true current density depends on the true geometrical area, which was estimated using the Zygo Mx post-processing software. The surface area of the four specimens compared to that of an ideally flat surface are also shown in Table 3. The S1 specimen has a significantly larger surface area, over 30 % than the ideally flat surface. The surface areas of the other three specimens are negligibly different, indicating that the current densities would be nearly the same, so the HE susceptibility can be compared directly. Caution should therefore be extended when comparing HE susceptibility of the S1 specimen, since the true current density is approximately ~30% lower.
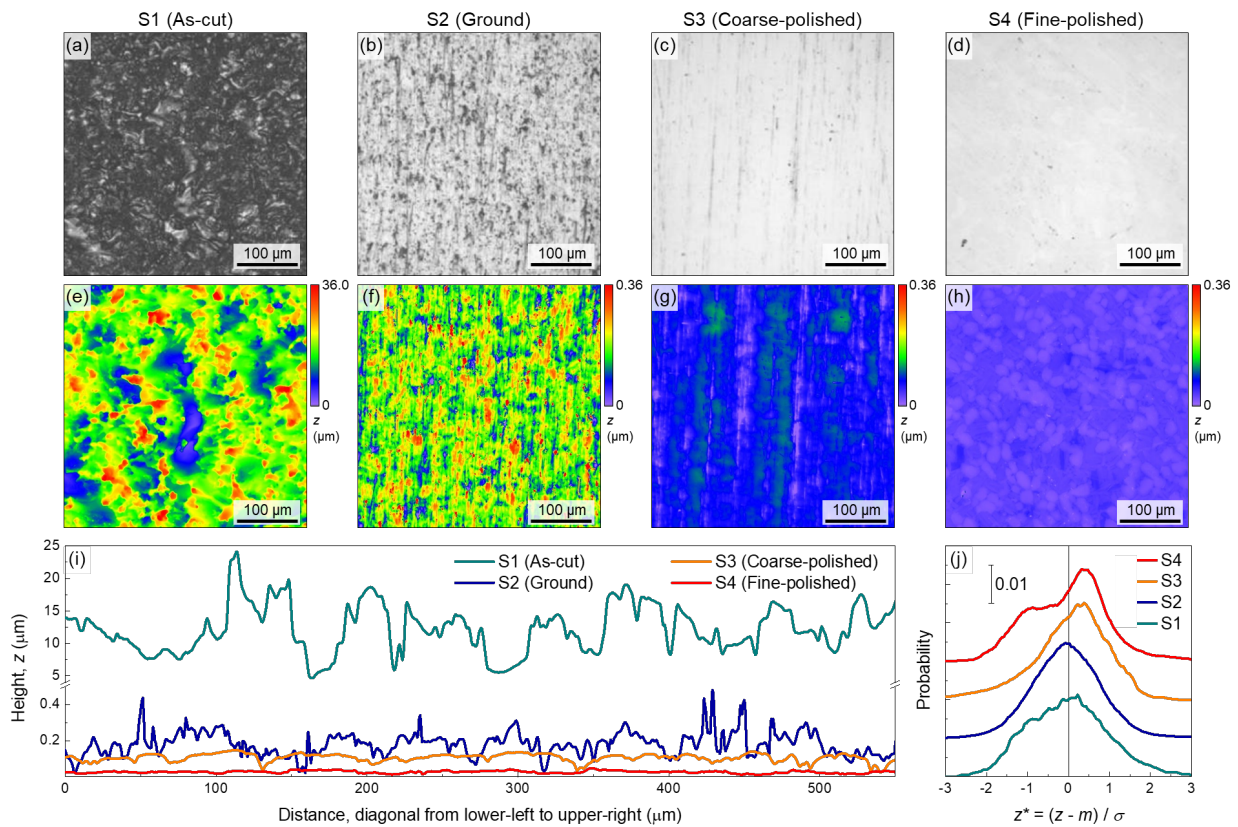
Figure 4. Optical microscopy images (a-d) and surface roughness maps (e-h) of the four specimen surfaces, (a,e) S1, As-cut, (b,f) S2, Ground, (c,g) S3, Coarse-polished, and (d,h) S4, Fine-polished. (i) Line profile of z-height values across the scan surfaces in the diagonal direction from lower-left to upper-right in (e-h). (j) Probability density distributions of z-height for the four specimens.

Table 3. Surface area, averaged surface roughness parameters and height distribution descriptor values obtained from the surface roughness maps in Figure 4.

Specimen	S1	S2	S3	S4
R_a (µm)	3.084×10^0	4.466×10^{-2}	1.471×10^{-2}	5.083×10^{-3}

13

R_q (μm)	1.829×10^1	6.240×10^{-2}	1.941×10^{-2}	6.503×10^{-3}
Sk	0.314	1.225	-0.958	-0.434
K	3.118	11.640	5.168	19.283
Surface area (% nominal)	131	100.31	100.0024	100.00051

Influences of surface finish on subsurface microstructures were investigated by electron microscopy imaging of cross-sections. The cut surface of S1 specimen retains perturbations induced by the rapid heating-cooling process during spark erosion of WEDM, as shown in Figure 5. A distinct and continuous surface layer, approximately 5μm in thickness, exists at the surface directly cut with WEDM. Such surface layers have been identified before, mostly in steels [41,42], formed due to the re-solidification of molten surface material during EDM. This re-cast layer has been termed the 'white layer' due to its appearance in the microscope [41,42]. Figure 5(b) shows the detailed microstructure of this layer, revealing fine, acicular laths which are 100-500 nm in thickness, which is typical of the α' (hcp) martensite. For this phase transformation to occur, the near-surface region would need to be cooled rapidly from above the β-transus at a rate exceeding the critical cooling rate for martensitic transformation (> 410 K s^{-1}) [43]. It is expected that WEDM fulfills this requirement, as the rapid heating and cooling cycles lead to repeated quenching of the subsurface region. The cooling rate Ti-6Al-4V experiences during water quenching is ~650 K s^{-1} [44], so this could lead to a martensitic transformation. Two martensite phases can be formed in Ti alloys (α' and α''), which can be distinguished by their crystal structure, since α' is hcp and α'' is orthorhombic [1]. As the EBSD phase map in Figure S3 (in Supplementary Materials) indicates, this phase was matched to hcp α (no EBSD phase file was available for α'), allowing the phase to be characterized as α' rather than α'', which agrees with the analysis from Stráský et al. [8]. Moreover, it is typically unexpected to form α'' in Ti-6Al-4V due to the usual requirement of a higher β stabilizer content; (> 9.4 wt.%. for vanadium) [1]. The transformation from β to α' is displacive, so occurs through a shear-type transformation in which the cooperative movement of atoms allows for a phase transformation without diffusion [1,3]. This transformation is facilitated by significant plastic deformation, resulting in the generation of interface dislocations and deformation twins [1,3,45]. Therefore, it is

14

346   reasonably expected that the S1 specimen contains a high dislocation density in the
347   subsurface area.
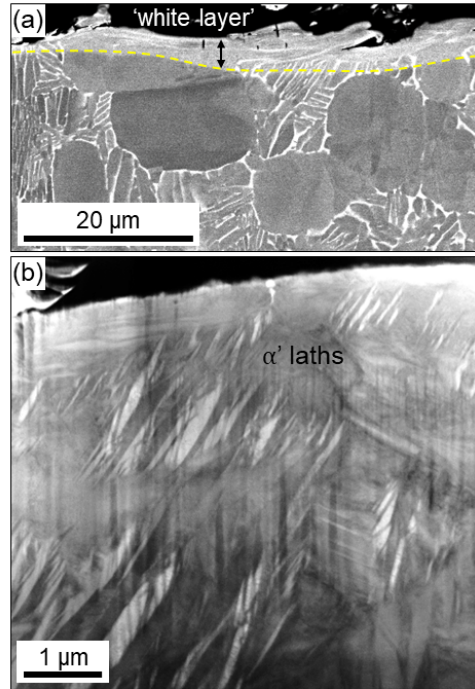
Figure 5. (a) BSE image of cross-section near the charging surface in the S1 specimen before H-charging. (b)
STEM dark-field image of the martensite laths in the 'white layer'.

351   Although grinding effectively removes the EDM white layer, it plastically deforms the
352   surface at a finer scale, as highlighted in the surface topography examination. Figure 6 shows
353   SEM electron channeling contrast (ECC) images and STEM micrographs of the S2 specimen
354   (a,b) and S4 specimen (c,d) before H-charging, respectively. The subsurface of the ground S2
355   specimen is still highly deformed compared to that of the polished S4 specimen, and exhibits
356   a large number of dislocation tangles in a depth of a few microns from the surface. This
357   clearly shows that the surface deformation during mechanical grinding is accommodated by
358   the generation of strain-induced dislocations, and further polishing procedures effectively
359   removes the deformed layer. It is important to note that the dislocation density has not been
360   quantified, and effects such as the dependence of α orientation on the active slip systems and
361   resulting dislocation response have not been considered here. However, considering the
362   considerable differences observed, it is clear that the non-polished specimens (S1 and S2)
363   are highly deformed, and this deformation level is significantly reduced during polishing.
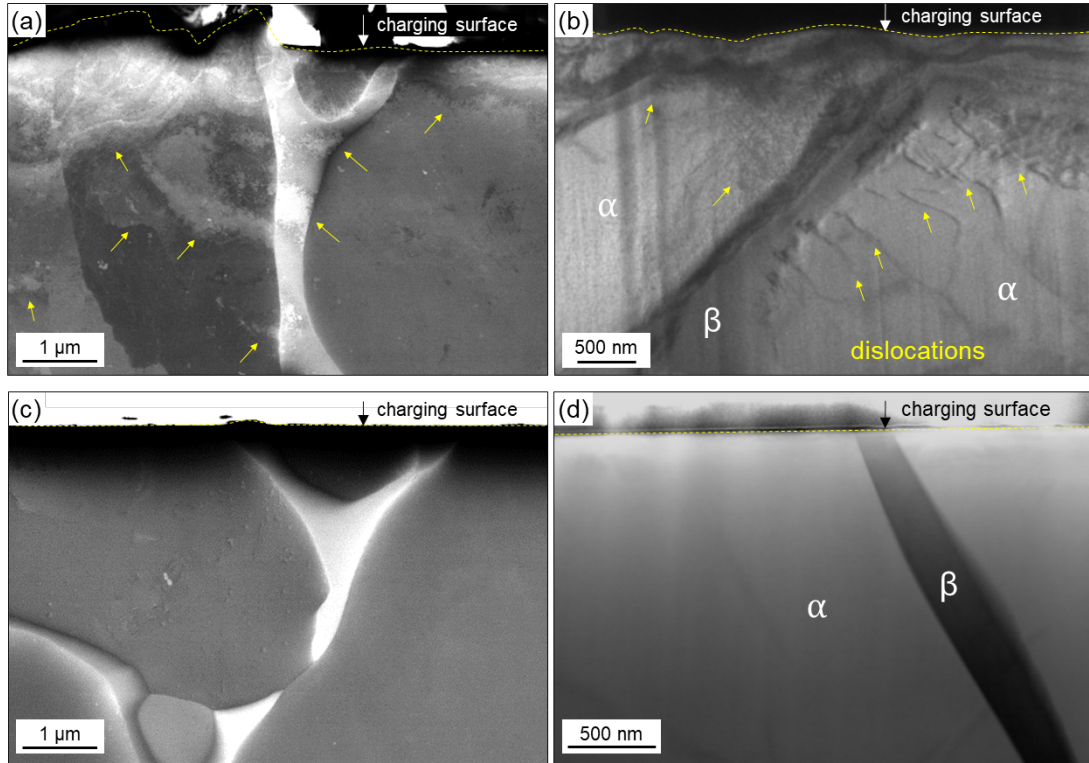
Figure 6. SEM ECC images (a,c) and STEM bright-field images (b,d) of cross-section near the charging surface. (a,b) S2 specimen. (c,d) S4 specimen. The yellow arrows in (a,b) highlight dislocation tangles and long dislocations in the subsurface.
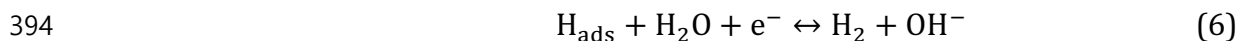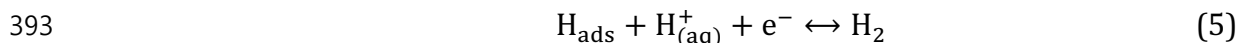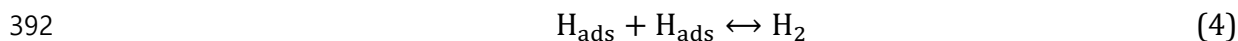
3.3. Hydrogen entry and subsurface diffusion

The assessments of microstructure and tensile deformation behavior have shown a clear difference in HE susceptibility between polished (S3 and S4) and non-polished (S1 and S2) specimens. The extensive hydride formation and resulting brittleness observed in the polished specimens suggest that H is readily able to enter the specimens and diffuse to nucleation sites for hydride formation (e.g. α/β boundaries). The non-polished specimens, however, seem to be protected under the employed charging conditions, showing no signs of HE. We used a direct observation of recombined hydrogen bubbles, TDS and SIMS to compare the amount of H-ingress and near-surface H-distribution. For these analyses, two representative specimens that show a significant difference in HE susceptibility were chosen for comparison; S2 (EDM and ground) and S4 (fine polished).

For H-charging in aqueous environment, all H products originate as protons (H^+) in

16

381   the electrolyte.   Reduction of protons at the reaction surface forms adsorbed hydrogen

382   atoms (H_{ads}), which can be bonded to the surface either weakly by physisorption or strongly

383   by chemisorption [13]. The electrochemical reduction process is described by Equation (2)

384   and (3).

385 $$H^+_{(aq)} + e^- \leftrightarrow H_{ads} \tag{2}$$

386 $$H_2O + e^- \leftrightarrow H_{ads} + OH^- \tag{3}$$
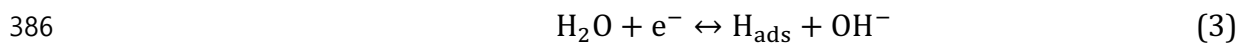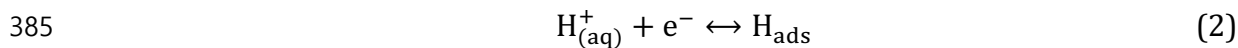
387   The adsorbed H then has three possible routes: (i) it may remain adsorbed on the

388   surface, (ii) it may be absorbed into the metal and cause HE, or (iii) it may recombine to form

389   molecular hydrogen (H_2) which would either dissolve in the aqueous solution or form gas

390   bubbles if the electrolyte solubility limit is exceeded [13]. The recombination reaction can

391   happen via the reactions described by Equation (4)-(6).

392 $$H_{ads} + H_{ads} \leftrightarrow H_2 \tag{4}$$

393 $$H_{ads} + H^+_{(aq)} + e^- \leftrightarrow H_2 \tag{5}$$

394 $$H_{ads} + H_2O + e^- \leftrightarrow H_2 + OH^- \tag{6}$$

395   Since the adsorbed H can only exist at surface sites (only as a monolayer), its

396   concentration is negligible in comparison to the concentration of absorbed H and

397   recombined H_2. We measured the amount of recombined H_2 using the optical microscope

398   combined with an electrochemical cell (Figure 7(a), See the Experimental Methodology

399   section for the details of the setup). A small specimen area exposed to the electrolyte in the

400   cell was directly observed through the slide glass cover and the electrolyte during

401   electrochemical H-charging, as shown in the OM images in Figure 7(b). The recombined H_2

402   bubbles were mostly trapped on the PTFE layer around its interface with the specimen, due

403   to the distinct wettability between them[1]. The amount of recombined H_2 molecules were

---

[1] The hydrophobic nature of PTFE (wetting angle θ = 118 - 165°, depending on the degree of elongation [54]) makes gas bubbles stay on the PTFE layer (to decrease the interface area between the PTFE and the aqueous electrolyte), while the hydrophilic Ti-6Al-4V surface (θ = 35° [55]) helps H_2 molecules formed on the sample easily migrate toward the PTFE. So the H_2 gas bubbles accumulate at the PTFE/sample interface, but it does not mean that the H recombination to H2 happens only at the interface.

404   estimated from the image analysis and the ideal gas law. The two-dimensional area (A_i) of the

405   bubbles in the images were analyzed using ImageJ software [46], and the volume of a bubble

406   (V_b) were estimated from the equivalent radius (r_{eq}) [47], which is the diameter of the circle

407   has the same area of the measured 2-D area of a single bubble ($A_i = \pi r_{eq}^2$, and $V_b = 4/3\ \pi r_{eq}^3$).

408   The total amount of H_2 recombination per area by H-charging time is plotted in Figure 7(c).

409   The rough surface of S2 specimen recombines a significantly larger amount of

410   electrochemically reduced H to H_2 molecules than the polished surface of S4 specimen. One

411   electron in the applied electric current reduces a proton to an atomic H, so the total amount

412   of H reduction and the percentage of H_2 recombination (or the percentage of H ingress in to

413   the specimen, inversely) can be calculated from the measured data, as plotted in Figure 7(d).

414   Only around 10-20% of atomic H among the total amount of reduced H diffuses into the S2

415   specimen and the rest is recombined into H_2 bubbles. In contrast, the S4 specimen absorbs

416   most of reduced H and less than 2 % of H turns into H_2 bubbles. One should note that the

417   range of H-charging time is very short compared to that applied to the tensile specimens and

418   the electrochemical reaction in this initial stage is not in steady state. Indeed, the percentage

419   of H ingress increases with H-charging time for the S2 specimen while it decreases for the S4

420   specimen. The gas volume estimation using the equivalent radius and the ideal gas law could

421   induce a certain level of error in these measurements. The H absorption rate at the surface

422   would also be influenced by the H content at the subsurface region. It is clear that,

423   nevertheless, the rough surface recombines more H to H_2 molecules and absorbs less atomic

424   H into the material, than the polished surface.
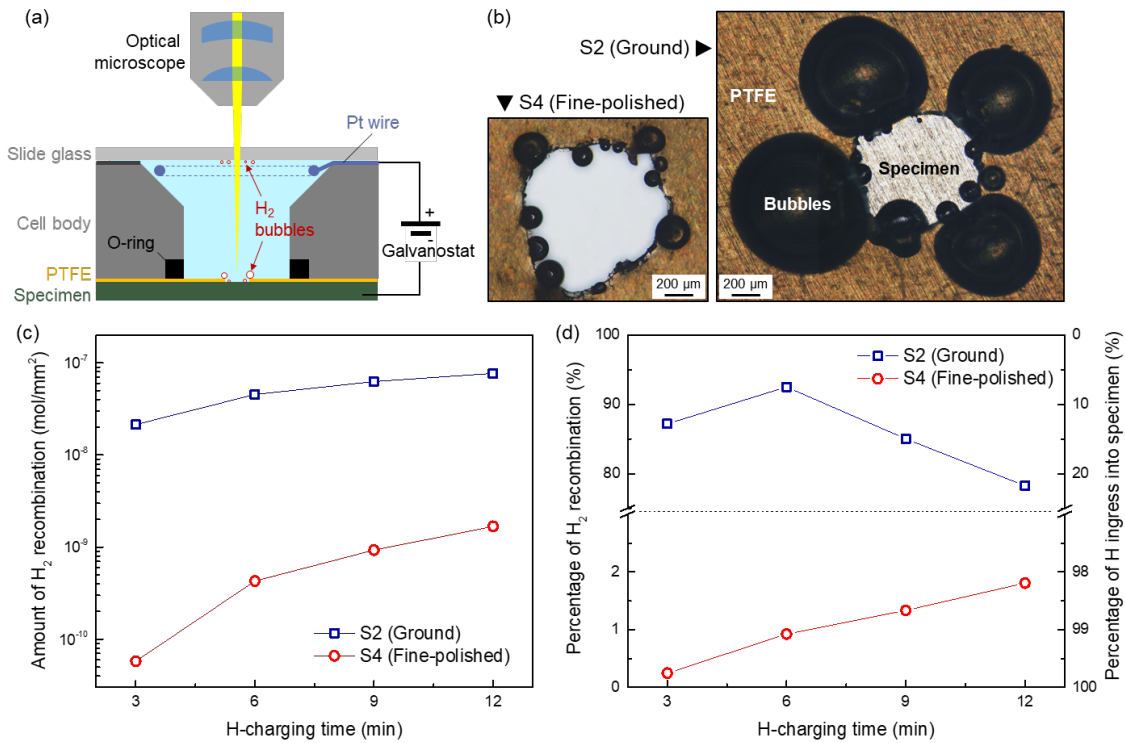
Figure 7. (a) Schematic diagram of the electrochemical cell combined with OM used for the direct analysis of H₂ bubbles. (b) OM images of H₂ bubbles around the H-charging area. Left: S4 specimen; Right: S2 specimen. (c) Amount of recombined H₂ molecules per area by H-charging time on the two specimens. (d) Percentages of H₂ recombination (left y-axis) and H ingress into specimen (right y-axis) in the total amount of electrochemical H reduction.

We also measured the amount of H absorbed in the S2 and S4 specimens by TDS after 40 h H-charging. Figure 8(a) shows the hydrogen partial pressure spectrum of the two specimens. The atomic fraction of H measured from the curves was 1258 ppm and 1519 ppm for S2 and S4 specimens, respectively, which reveals that the polished specimen absorbed ~20 % more H than the ground specimen. Figure 8(b,c) presents the deconvoluted desorption peaks of each curve. The S4 specimen clearly exhibits two major peaks, of which maxima are located at 566 °C (Peak 1) and 668 °C (Peak 2), respectively. The curve of S2 specimen has one major peak at 663 °C and a small peak (Peak 3) at 815 °C at the right shoulder of the major peak. Given the similarity of peak position and shape, the major peak can be considered to be the same with Peak 2 in Figure 8(b). H in this bimodal Ti-6Al-4V alloy diffuses through the β phase first, and starts to form the hydride phase in the α phase from the α/β interface when the β phase is saturated with H at a certain level [10,39]. This indicates that the Peak 2 that appears in the both curves originates from H stored in the β

19

phase. Given that the hydride phase were observed in the H-charged S4 specimen (Figure 2(h) and Figure 3) but not in the S2 specimen, H signal related to Peak 1 comes from the decomposition of the hydride. The small amount of H related to Peak 3 that is observed only in the rough specimen is expected to originate from H trapped in the high-density defects in the subsurface region (Figure 6(a)), which will be further discussed with the SIMS results later. The TDS results suggests that the S2 specimen with the rough surface absorbs less H and H stored in the β phase does not induce a significant embrittlement in this alloy.
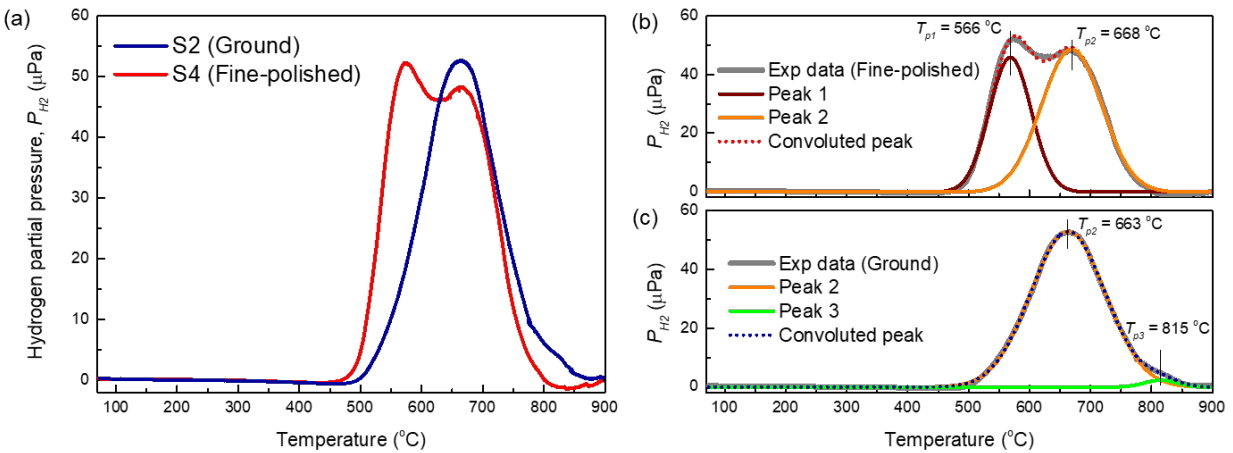
Figure 8. (a) H_2 partial pressure-temperature curves of H-charged S2 and S4 specimens, measured by TDS. (b-c) Deconvolution of each curve to individual Gaussian peaks - (b) S4 specimen, (c) S2 specimen.

In addition to the surface roughness effect, the differences in subsurface deformation observed earlier would influence H diffusion flux in the subsurface, given that H is readily trapped at defects [14,48]. In order to compare the H content in the subsurface region SIMS was performed on the S2 and S4 specimens after H-charging. Ramp specimens inclined at 10° to the charging surface (Figure 9(a) and (c)) were ion-milled so that the H content could be compared with depth into the specimen. In order to protect the charging surface, a Ni layer was electrodeposited on the surface before ion-milling. The H⁻ ion maps in Figure 9(b) and (d) were taken in the local regions near the charging surface which are marked with rectangles in Figure 9(a) and (c). The H⁻ signal in the ion maps were normalized by the total ion signal to remove surface effects. The brighter contrast in the left part of Figure 9(b) than that of Figure 9(d) indicates higher H concentration in the subsurface region under the ground surface compared to under the fine-polished surface. Line profiles along the

466   horizontal directions in the H⁻ ion signal maps show the difference more clearly, which are

467   plotted in Figure 9(d). The H content increases quite considerably in the Ti-6Al-4V specimens

468   in both cases compared to the protective Ni layer, suggesting that a considerable amount of

469   the H remains irreversibly trapped in the specimens after H-charging. The H content is nearly

470   twice as high for the S2 specimen compared to the S4 specimen, which reveals an interesting

471   difference considering the other two analyses previously suggested in this section. Despite

472   the recombined H_2 bubble analysis and TDS measurements suggesting that less H is

473   absorbed by the S2 specimen, it appears to have a considerably higher subsurface H

474   concentration than the S4 specimen, which corresponds to the Peak 3 observed in its TDS

475   result. (Figure 8(c)). The thicknesses of the H-accumulated layer and the deformed layer in

476   the subsurface region in the S2 specimen are not directly compared here, because (i) the

477   measured depth in the SIMS experiment was limited and (ii) the degree of subsurface

478   deformation is not uniform, as shown in the grains in Figure 6(a). However, given that the

479   only difference in the subsurface microstructure between the S2 and S4 specimens is the

480   degree of deformation (or defect density), it is reasonable to suppose that the high defect

481   density in the subsurface region causes the high H concentration detected in the SIMS

482   measurement[2]. It is worth noting that hydrogen absorbed into the Ti-6Al-4V alloy first

483   diffuses through the β phase and forms a solid solution with the β phase by occupying

484   tetrahedral interstitial sites [10,39]. Even in the subsurface region with high-density

485   dislocations, the β phase would be still the primary accumulation site for hydrogen as shown

486   by TDS Peak 2 in Figure 8(c), but the high-density dislocations provide additional trapping

487   sites for hydrogen, as suggested by Peak 3 in Figure 8(c).

---

[2] Despite H-accumulation in the deformed subsurface region, no evidence of brittle cracking was observed in the subsurface region of the S2 specimen (See Figure SI6 in Supplementary Materials). This might originate from either the high HE resistance of beta phase (because the majority of hydrogen exists in the beta phase) or the effect of high-density dislocations that distribute H more uniformly over the microstructure, which requires further investigation.
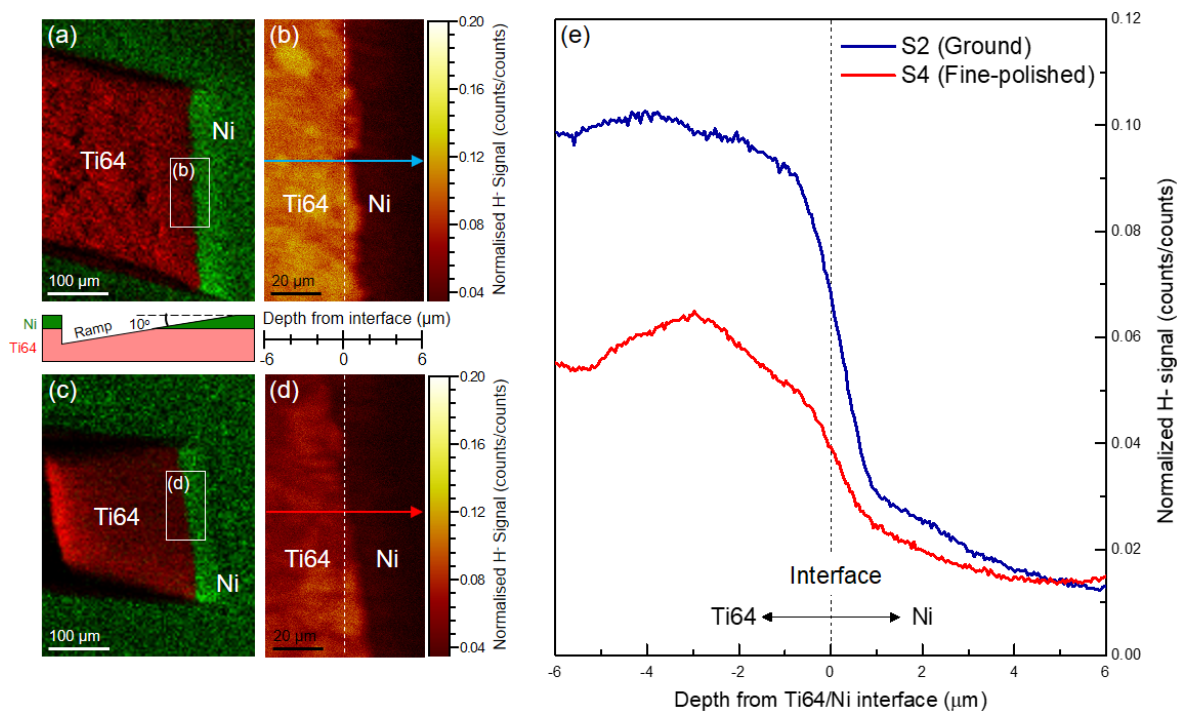
Figure 9. SIMS ion maps for (a,b) S2 specimen and (c,d) S4 specimen. (a) and (c) shows overlay of ion maps for Ti (TiO⁻ signal, red) and Ni (NiO⁻ signal, green). (b) and (d) show ion maps of normalized H⁻ signal. The schematic diagram between a and c describes the ramp morphology, and the scale bar between (b) and (d) shows depth from the Ni/Ti-6Al-4V interface in the ramp along the horizontal position in the H⁻ signal maps. (e) Line profiles of normalized H⁻ signal along the horizontal arrow lines in (b) and (d).

4. Discussion

The experimental results clearly present that the roughened surfaces in both the S1 and S2 specimens hinder H-absorption into them and assists in maintaining their ductility even after a harsh electrochemical exposure to hydrogen. In contrast, specimens S3 and S4 with polished surfaces exhibit extensive hydride formation and consequent embrittlement, as previously reported [10]. We investigated the influence of surface state on H-absorption processes by separating the possible factors into two; electrochemical activity change by surface roughness and enhanced H-trapping by subsurface deformation. The possibility of formation of a thicker oxide layer that can act as a H-permeation barrier on the S1 and S2 surfaces was ruled out by STEM-EDS analyses (See Supplementary Materials). Other factors such as local composition or crystallographic orientation that are known to influence the electrochemical properties of catalysts [49,50] are not considered here, because H-charging

22

507 in this study was performed on millimeter-scale areas of the Ti-6Al-4V alloy without a strong
508 crystallographic texture; in the present case all the specimens will have had identical textures
509 in any case.

510   Considering the previous observations on the effects of deformation on corrosion
511 behavior of different metals [19–21], surface roughness should alter electrochemical activity.
512 From a simple fact that a rougher surface has a larger surface area (Table 3), one could expect
513 a higher H-flux through the surface. However, the H_2 bubble analysis in Figure 7 clearly
514 demonstrates that the rough surface induces a higher fraction of recombination to H_2 gas
515 (Equations 4-6) – in other words, a smaller fraction of atomic hydrogen is absorbed into the
516 surface. Under constant current control (employed for all H-charging processes in this study),
517 the rate of total H^+ reduction at the cathode is same for all specimens but the higher activity
518 at the rough surface promotes only the recombination reactions, which reduces the amount
519 of H absorption that causes embrittlement.

520   It is intriguing that the HE behavior in these specimens shows such a pronounced
521 change between the two groups; non-polished specimens (S1 and S2) and polished
522 specimens (S3 and S4). The estimated surface area values in Table 3 ($\sim$ 30% larger, and only
523 in sample S1) suggests that roughening-induced increase of surface area would not be a
524 critical factor in the hydrogen uptake in this alloy. Similarly, the difference in average
525 roughness, either R_a or R_q, between specimens S1 and S2 is a few orders of magnitude larger
526 than that between the S2 and S3 specimens. This also implies that the average roughness (or
527 height difference between peaks and valleys) does not play a decisive role in the
528 improvement of HE resistance. The average roughness values do not provide any information
529 about shape and distribution of asperities (i.e. peaks and valleys) that are influential to local
530 electron flux [16]. As mentioned in Section 3.2, skewness (Sk) and kurtosis (K) describes an
531 asymmetry of probability distribution and represent distribution of peaks and valleys in a
532 surface roughness profile [40]. The surface profiles of the four specimens investigated in this
533 study can be categorized with the Sk and K values, as described schematically in Figure 10. A
534 negative Sk value indicates a shift of probability distribution to +z direction from the origin.
535 This means a larger number of height values above the average height, which represents a
536 topography with relatively wide plateaus above the average height. The remaining minor

number of height values below the average represents surface valleys. In other words, a negative Sk indicates a surface dominated by valleys over peaks. For a positive Sk value, the wide plateaus are above the mean height and peaks dominate over valleys. K is a measure of peak and valley sharpness within the surface roughness profile. A symmetric Gaussian distribution has $K = 3$. A large K value above 3 indicates a pointed probability distribution, and sharper peaks and valleys in the surface profile. The clear division of Sk values into the two groups of non-polished samples (positive) and polished samples (negative) indicates that the existence of pronounced peaks plays a critical role in promoting the H-recombination reaction and reducing the amount of H-uptake. In other words, a few scratches on a flattened surface as the case of S3 specimen are not able to efficiently reduce H-uptake even though they increase the average roughness. The decreased electron work function at peaks [16] could promote a higher density of hydrogen reduction compared to a flat surface, and the excess amount of adsorbed hydrogen (H_{ads}) at the peaks recombines easily into H_2 molecules. The influence of peak (or valley) sharpness represented by K was not clear in the HE behavior in the tested condition of this study. Given that sharper peaks have a smaller work function [16], the peak sharpness might also influence the H-uptake behavior of rough surfaces (especially in long-term H-ingress), which requires further study.
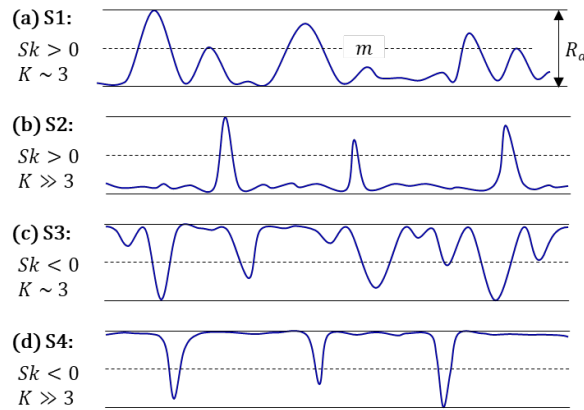
Figure 10. Schematic illustration for surface roughness profiles with different skewness (Sk) and kurtosis (K), in the cases of specimens S1 to S4. R_a and m is the arithmetic mean roughness and mean height, respectively.

Grinding generates a high density of dislocations by plastically deforming the surface, and subsequent polishing processes using diamond or silica suspensions effectively remove the deformed subsurface layer, as shown in Figure 6. The EDM white layer with α' martensite

in the S1 specimen in Figure 5a also contains a high density of lath boundaries as well as geometrically necessary dislocations for accommodating a small angular deviation in crystallographic orientation between the laths (or between the laths and matrix). Grain boundaries, lath boundaries and dislocations are effective H-trapping sites, serving as sinks which accumulate H and reduce the effective diffusion coefficient [14,48,51]. The high density of H-trapping sites in the subsurface region hinders not only H-diffusion into the material interior but also H-absorption at the surface. The net flux of hydrogen atoms absorbed into the metal can be described by Equation 8 [12],

$$J(\mathrm{H_{abs}}) = k_{abs} A_T \theta_{ad} - k_{des} C_0 (1 - \theta_{ad}) \qquad (8)$$

where θ_{ad} is the surface coverage of adsorbed hydrogen atoms, k_{abs} and k_{des} are the absorption and desorption rate constants respectively, A_T is an Arrhenius term dependent on hydrostatic stress, and C_0 is the sub-surface lattice hydrogen concentration. A greater trap density underneath the roughened surfaces would result in a higher C_0, as shown by the SIMS results in Figure 9, reducing the H-absorption flux. A higher recombination ratio on the surface would decrease the amount of surface-adsorbed hydrogen (θ_{ad}), further reducing the net H-uptake flux.

Considering the results of comprehensive analyses of H recombination and uptake in Section 3.3, the enhanced HE-resistance of roughened specimens against electrochemical H-charging can be summarized as shown in Figure 11. Polishing reduces the electrochemical activity of the surface, which decreases the recombination ratio and means more H is available for entry into the material. The polishing treatment also reduces the subsurface deformation and decreases the density of defects that act as H-trapping sites. On the other hand, a rough surface (dominated by peaks) such as the as-cut or as-ground states promotes the recombination reaction, reducing the amount of absorbable hydrogen at the surface. The higher density of H-trapping sites from subsurface deformation decreases the thermodynamic driving force for H entry due to a reduced H concentration gradient across the electrolyte-metal interface, as well as a decrease in the effective H-diffusivity in the deformed subsurface region. H accumulation in the deformed subsurface would induce a large concentration gradient of H that eventually drives H diffusion to the material interior,

589 but the internal stress gradient between the subsurface and the interior can hinder H
590 diffusion further [52].

591 It is proposed that these effects combine to impede both H entry and transport when
592 the alloy surface is roughened, which leads to improved HE-resistance during the employed
593 electrochemical H-charging. It is worth noting that similar phenomena were reported for Ti-
594 6Al-4V specimens in a gaseous H environment at 650 °C [53] – a polished specimen forms
595 TiH_2 hydride while a rough ground one does not in the same condition, which was mainly
596 attributed to a higher oxygen concentration at the ground surface than the polished surface.
597 The influences of roughness and subsurface defects were not considered in the reference
598 [53]. However, H-uptake from gaseous hydrogen is a competition between H_2 dissociation
599 and recombination, so it might be possible that the rough surface also promotes H
600 recombination even in gaseous hydrogen environments. Regardless of the hydrogen source,
601 defects underneath the rough surface could trap H unless the temperature is high enough to
602 induce thermal atomic vibration that overcomes the trapping energy of the defects. Further
603 studies are needed for investigating clearly the effects of surface finish on H-uptake in a
604 gaseous hydrogen environment.
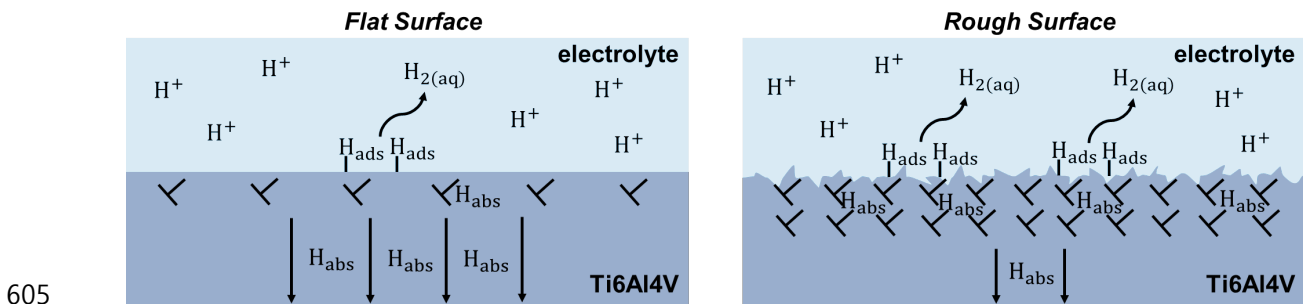
Figure 11. Representation of H behavior at polished flat surfaces and non-polished rough surfaces with surface peaks. The rough surface is more active for recombination of H_{ads} into H_2 due to the surface peaks and less H enters the material. The higher density of dislocations under the rough surface also increases the amount of trapped H in the subsurface volume, which blocks H_{abs} diffusion further into the sample.

5. Conclusions

612 The susceptibility of Ti-6Al-4V to HE in electrochemical H-charging has been
613 investigated and compared among specimens with different surface finishes achievable

614　through standard preparation techniques. A major difference in HE susceptibility was
615　observed between polished and non-polished specimens: upon electrochemical H-charging,
616　polished specimens are significantly more susceptible to HE, while the non-polished ones
617　with roughened surfaces do not show a clear reduction in ductility compared to uncharged
618　material. The direct observation analysis of recombined H_2 bubbles and TDS analysis
619　revealed that the roughened surface with protruded surface peaks exhibits a higher
620　electrochemical activity than a polished flat surface, which increases the H recombination
621　ratio and reduces the H-ingress flux. This causes a significantly smaller amount of atomic H
622　to be absorbed by the rough surface at constant current, than by the polished surface. In
623　addition to the change in H-recombination ratio, surface roughening induces a higher density
624　of defects, or H-trapping sites, which decreases the effective H-diffusivity as well as hinders
625　H-ingress by decreasing the concentration gradient at the metal-electrolyte interface. These
626　combined effects resulting from the increased roughness of the surface provide the enhanced
627　resistance against HE in the aqueous electrochemical H-environment by impeding H-
628　transport to the material interior.

629　　　　The implications of these findings are notable both for researchers conducting H-
630　charging experiments, and for industries concerned with aqueous HE in service. For the
631　former, this work has shown that the specimen surface conditions are crucial in experimental
632　design, and that even small changes to preparation processes can have significant effects on
633　H-uptake. Thus, when comparing HE after electrochemical charging, it is essential to ensure
634　minimal variation in surface preparation procedures among samples. In the case of the latter,
635　these results highlight new opportunities. Surface treatments such as etching, machining and
636　polishing are already widely used to address fatigue, wear and corrosion challenges. For
637　components exposed to aqueous hydrogen environments, HE susceptibility is an additional
638　concern that, based on our results, can be addressed by engineering the surface roughness.

639

645

References

647   [1]   G. Lütjering, J.C. Williams, Titanium, Springer Berlin Heidelberg, Berlin, Heidelberg,
648   2003. https://doi.org/10.1007/978-3-540-71398-2.

649   [2]   T.P. Chapman, D. Dye, D. Rugg, Hydrogen in Ti and Zr alloys: industrial perspective,
650   failure modes and mechanistic understanding., Philos. Trans. A. Math. Phys. Eng. Sci.
651   375 (2017) 20160418. https://doi.org/10.1098/rsta.2016.0418.

652   [3]   C. Leyens, M. Peters, Titanium and Titanium Alloys, Wiley-VCH Verlag GmbH & Co.
653   KGaA, Weinheim, FRG, 2003. https://doi.org/10.1002/3527602119.

654   [4]   D. Hardie, E.A. Charles, A.H. Lopez, Hydrogen embrittlement of high strength pipeline
655   steels, Corros. Sci. 48 (2006) 4378–4385.
656   https://doi.org/10.1016/j.corsci.2006.02.011.

657   [5]   J.R. Sims, 6 - Standards and codes to control hydrogen-induced cracking in pressure
658   vessels and pipes for hydrogen gas storage and transport, in: Gaseous Hydrogen
659   Embrittlement of Materials in Energy Technologies, Woodhead Publishing, 2012: pp.
660   177–192. https://doi.org/https://doi.org/10.1533/9780857093899.1.177.

661   [6]   J.R. Myers, J.A. Hall, Hot Salt Stress Corrosion Cracking of Titanium Alloys: An
662   Improved Model for the Mechanism, Corrosion. 33 (1977) 252–257.

663   [7]   D. Sinigaglia, G. Taccani, B. Vicentini, Hot-salt-stress-corrosion cracking of titanium
664   alloys, Corros. Sci. 18 (1978) 781–796. https://doi.org/10.1016/0010-
665   938X(78)90015-X.

666   [8]   D. Eliezer, T.H. Böllinghaus, 18 - Hydrogen effects in titanium alloys, in: R.P. Gangloff,
667   B.P. Somerday (Eds.), Gaseous Hydrogen Embrittlement of Materials in Energy
668   Technologies, Vol. 2, Woodhead Publishing, 2012: pp. 668–706.
669   https://doi.org/10.1533/9780857093899.3.668.

670   [9]   S. Joseph, T.C. Lindley, D. Dye, E.A. Saunders, The mechanisms of hot salt stress
671   corrosion cracking in titanium alloy Ti-6Al-2Sn-4Zr-6Mo, Corros. Sci. 134 (2018)
672   169–178. https://doi.org/10.1016/j.corsci.2018.02.025.

673   [10]   J. Kim, E. Plancher, C.C. Tasan, Hydrogenation-induced lattice expansion and its
674   effects on hydrogen diffusion and damage in Ti-6Al-4V, Acta Mater. 188 (2020) 686–
675   696. https://doi.org/10.1016/j.actamat.2020.02.029.

676   [11]   E. Conforto, I. Guillot, X. Feaugas, Solute hydrogen and hydride phase implications on

677 the plasticity of zirconium and titanium alloys: a review and some recent advances,
678 Philos. Trans. R. Soc. A Math. Phys. Eng. Sci. 375 (2017) 20160417.
679 https://doi.org/10.1098/rsta.2016.0417.

680 [12] A. Turnbull, Perspectives on hydrogen uptake, diffusion and trapping, Int. J.
681 Hydrogen Energy. 40 (2015) 16961–16970.
682 https://doi.org/10.1016/J.IJHYDENE.2015.06.147.

683 [13] A. Turnbull, 4 - Hydrogen diffusion and trapping in metals, in: Gaseous Hydrogen
684 Embrittlement of Materials in Energy Technologies: Mechanisms, Modelling and
685 Future Developments, Woodhead Publishing, 2012: pp. 89–128.
686 https://doi.org/10.1016/B978-0-85709-536-7.50004-0.

687 [14] H.K.D.H. Bhadeshia, Prevention of Hydrogen Embrittlement in Steels, ISIJ Int. 56
688 (2016) 24–36. https://doi.org/10.2355/isijinternational.ISIJINT-2015-430.

689 [15] J.H. Holbrook, H.J. Cialone, E.W. Collings, E.J. Drauglis, P.M. Scott, M.E. Mayfield, 5 -
690 Control of hydrogen embrittlement of metals by chemical inhibitors and coatings, in:
691 Gaseous Hydrogen Embrittlement of Materials in Energy Technologies, Woodhead
692 Publishing, 2012: pp. 129–153.
693 https://doi.org/https://doi.org/10.1533/9780857095374.1.129.

694 [16] W. Li, D.Y. Li, Influence of surface morphology on corrosion and electronic behavior,
695 Acta Mater. 54 (2006) 445–452. https://doi.org/10.1016/j.actamat.2005.09.017.

696 [17] D.L. Dull, L. Raymond, Thermal and Mechanical Effects on the Corrosion Behavior of
697 Ti-6Al-4V Alloy, J. Electrochem. Soc. 120 (1973) 1632.
698 https://doi.org/10.1149/1.2403319.

699 [18] A. Chandra, J.J. Ryu, P. Karra, P. Shrotriya, T. Weik, Electrochemical dissolution of
700 biomedical grade Ti6Al4V: Influence of stress and environment, CIRP Ann. - Manuf.
701 Technol. 58 (2009) 499–502. https://doi.org/10.1016/j.cirp.2009.03.114.

702 [19] H. Krawiec, V. Vignal, E. Schwarzenboeck, J. Banasa, Role of plastic deformation and
703 microstructure in the micro-electrochemical behaviour of Ti-6Al-4V in sodium
704 chloride solution, Electrochim. Acta. 104 (2013) 400–406.
705 https://doi.org/10.1016/j.electacta.2012.12.029.

706 [20] Z. Cui, Z. Liu, L. Wang, X. Li, C. Du, X. Wang, Effect of plastic deformation on the
707 electrochemical and stress corrosion cracking behavior of X70 steel in near-neutral
708 pH environment, Mater. Sci. Eng. A. 677 (2016) 259–273.
709 https://doi.org/10.1016/j.msea.2016.09.033.

710 [21] J. Gravier, V. Vignal, S. Bissey-Breton, Influence of residual stress, surface roughness
711 and crystallographic texture induced by machining on the corrosion behaviour of
712 copper in salt-fog atmosphere, Corros. Sci. 61 (2012) 162–170.
713 https://doi.org/10.1016/j.corsci.2012.04.032.

714 [22] I. Herraiz-Cardona, E. Ortega, J.G. Antón, V. Pérez-Herranz, Assessment of the

715 roughness factor effect and the intrinsic catalytic activity for hydrogen evolution
716 reaction on Ni-based electrodeposits, Int. J. Hydrogen Energy. 36 (2011) 9428–9438.
717 https://doi.org/10.1016/j.ijhydene.2011.05.047.

718 [23] A.P. Brown, M. Krumpelt, R.O. Loutfy, N.P. Yao, The effect of surface roughness on the
719 hydrogen evolution reaction kinetics with mild steel and nickel cathodes,
720 Electrochim. Acta. 27 (1982) 557–560. https://doi.org/10.1016/0013-
721 4686(82)85039-1.

722 [24] H. Hamzah, A.T. Kuhn, The role of surface texture and anode-cathode size ratios on
723 mass transfer in undivided electrochemical reactors, J. Appl. Electrochem. 10 (1980)
724 635–647. https://doi.org/10.1007/BF00615487.

725 [25] A.T. Kuhn, J. Bin Yusof, P. Hogan, The role of electrode structure and surface texture
726 in the performance of gas evolving electrodes, J. Appl. Electrochem. 9 (1979) 765–
727 775. https://doi.org/10.1007/BF00614972.

728 [26] H. Dehmani, C. Brugger, T. Palin-Luc, C. Mareau, S. Koechlin, Experimental study of
729 the impact of punching operations on the high cycle fatigue strength of Fe-Si thin
730 sheets, Int. J. Fatigue. 82 (2016) 721–729.
731 https://doi.org/10.1016/j.ijfatigue.2015.09.030.

732 [27] A. Lara, I. Picas, D. Casellas, Effect of the cutting process on the fatigue behaviour of
733 press hardened and high strength dual phase steels, J. Mater. Process. Technol. 213
734 (2013) 1908–1919. https://doi.org/10.1016/j.jmatprotec.2013.05.003.

735 [28] J.P.M. Hoefnagels, C. Du, C. Cem Tasan, Laser-induced toughening inhibits cut-edge
736 failure in multi-phase steel, Scr. Mater. 177 (2020) 79–85.
737 https://doi.org/10.1016/j.scriptamat.2019.09.022.

738 [29] ASTM B265-15, Standard Specification for Titanium and Titanium Alloy Strip, Sheet,
739 and Plate, ASTM International, West Conshohocken, PA, 2015.

740 [30] J. Kim, C.C. Tasan, Microstructural and micro-mechanical characterization during
741 hydrogen charging: An in situ scanning electron microscopy study, Int. J. Hydrogen
742 Energy. 44 (2019) 6333–6343. https://doi.org/10.1016/J.IJHYDENE.2018.10.128.

743 [31] C.L. Briant, Z.F. Wang, N. Chollocoop, Hydrogen embrittlement of commercial purity
744 titanium, Corros. Sci. 44 (2002) 1875–1888. https://doi.org/10.1016/S0010-
745 938X(01)00159-7.

746 [32] G.A. Young, J.R. Scully, Effects of hydrogen on the mechanical properties of a Ti-Mo-
747 Nb-Al alloy, Scr. Metall. Mater. 28 (1993) 507–512. https://doi.org/10.1016/0956-
748 716X(93)90091-6.

749 [33] D.A. Hardwick, D.G. Ulmer, Effect of Hydrogen on the Microstructure and Mechanical
750 Properties of the Ti Alloy: Ti-15Mo-3Nb-3Al-0.2Si, in: A.W. Thompson, N.R. Moody
751 (Eds.), Hydrogen Effects in Materials, TMS, Hoboken, NJ, USA, 1996: pp. 735–744.
752 https://doi.org/10.1002/9781118803363.ch63.

753   [34]   K. Kumar, A. Pooleery, K. Madhusoodanan, R.N. Singh, J.K. Chakravartty, B.K. Dutta,
754   R.K. Sinha, Use of miniature tensile specimen for measurement of mechanical
755   properties, Procedia Eng. 86 (2014) 899–909.
756   https://doi.org/10.1016/j.proeng.2014.11.112.

757   [35]   X.-Q. Wang, J.-T. Wang, Structural stability and hydrogen diffusion in TiHx alloys,
758   Solid State Commun. 150 (2010) 1715–1718.
759   https://doi.org/10.1016/J.SSC.2010.06.004.

760   [36]   Y. Chang, W. Lu, J. Guénolé, L.T. Stephenson, A. Szczpaniak, P. Kontis, A.K. Ackerman,
761   F.F. Dear, I. Mouton, X. Zhong, S. Zhang, D. Dye, C.H. Liebscher, D. Ponge, S. Korte-
762   Kerzel, D. Raabe, B. Gault, Ti and its alloys as examples of cryogenic focused ion beam
763   milling of environmentally-sensitive materials, Nat. Commun. 10 (2019) 942.
764   https://doi.org/10.1038/s41467-019-08752-7.

765   [37]   O.T. Woo, G.C. Weatherly, C.E. Coleman, R.W. Gilbert, The precipitation of γ-
766   deuterides (hydrides) in titanium, Acta Metall. 33 (1985) 1897–1906.
767   https://doi.org/10.1016/0001-6160(85)90011-2.

768   [38]   H.E. Weekes, V.A. Vorontsov, I.P. Dolbnya, J.D. Plummer, F. Giuliani, T.B. Britton, D.
769   Dye, In situ micropillar deformation of hydrides in Zircaloy-4, Acta Mater. 92 (2015)
770   81–96. https://doi.org/10.1016/j.actamat.2015.03.037.

771   [39]   J. Kim, J. Kang, C.C. Tasan, Hydride formation in Ti6Al4V : An in situ synchrotron X-
772   ray diffraction study, Scr. Mater. 193 (2021) 12–16.
773   https://doi.org/10.1016/j.scriptamat.2020.10.025.

774   [40]   B. Bhushan, Surface roughness analysis and measurement techniques, in: B. Bhushan
775   (Ed.), Modern Tribology Handbook: Volume One: Principles of Tribology, CRC Press,
776   Boca Raton, FL, USA, 2000: pp. 49–119.
777   https://doi.org/10.1201/9780849377877.ch2.

778   [41]   G. Cusanelli, A. Hessler-Wyser, F. Bobard, R. Demellayer, R. Perez, R. Flükiger,
779   Microstructure at submicron scale of the white layer produced by EDM technique, J.
780   Mater. Process. Technol. 149 (2004) 289–295.
781   https://doi.org/10.1016/j.jmatprotec.2003.11.047.

782   [42]   B. Ekmekci, Residual stresses and white layer in electric discharge machining (EDM),
783   Appl. Surf. Sci. 253 (2007) 9234–9240.
784   https://doi.org/10.1016/j.apsusc.2007.05.078.

785   [43]   T. Ahmed, H.J. Rack, Phase transformations during cooling in α + β titanium alloys,
786   Mater. Sci. Eng. A. 243 (1998) 206–211. https://doi.org/10.1016/s0921-
787   5093(97)00802-2.

788   [44]   H. Galarraga, R.J. Warren, D.A. Lados, R.R. Dehoff, M.M. Kirka, P. Nandwana, Effects of
789   heat treatments on microstructure and properties of Ti-6Al-4V ELI alloy fabricated
790   by electron beam melting (EBM), Mater. Sci. Eng. A. 685 (2017) 417–428.

791   https://doi.org/10.1016/j.msea.2017.01.019.

792   [45]   P. Barriobero-Vila, J. Gussone, A. Stark, N. Schell, J. Haubrich, G. Requena, Peritectic
793   titanium alloys for 3D printing, Nat. Commun. 9 (2018) 3426.
794   https://doi.org/10.1038/s41467-018-05819-9.

795   [46]   W.S. Rasband, ImageJ, (n.d.).

796   [47]   R.C. Darton, R.D. LaNauze, J.F. Davidson, D. Harrison, Bubble Growth Due To
797   Coalescence in Fluidised Beds, Trans Inst Chem Eng. 55 (1977) 274–280.

798   [48]   A.J. Kumnick, H.H. Johnson, Deep Trapping States for Hydrogen in Deformed Iron,
799   Acta Metall. 28 (1980) 33–39.

800   [49]   E. Skúlason, V. Tripkovic, M.E. Björketun, S. Gudmundsdóttir, G. Karlberg, J.
801   Rossmeisl, T. Bligaard, H. Jónsson, J.K. Nørskov, Modeling the electrochemical
802   hydrogen oxidation and evolution reactions on the basis of density functional theory
803   calculations, J. Phys. Chem. C. 114 (2010) 18182–18197.
804   https://doi.org/10.1021/jp1048887.

805   [50]   M. Liu, D. Qiu, M.C. Zhao, G. Song, A. Atrens, The effect of crystallographic orientation
806   on the active corrosion of pure magnesium, Scr. Mater. 58 (2008) 421–424.
807   https://doi.org/10.1016/j.scriptamat.2007.10.027.

808   [51]   F.G. Wei, K. Tsuzaki, 13 - Hydrogen trapping phenomena in martensitic steels, in:
809   Gaseous Hydrogen Embrittlement of Materials in Energy Technologies, Woodhead
810   Publishing, 2012: pp. 493–525.
811   https://doi.org/https://doi.org/10.1533/9780857093899.3.493.

812   [52]   J.L. Waisman, R. Toosky, G. Sines, Uphill diffusion and progressive embrittlement:
813   hydrogen in titanium, Metall. Trans. A. 8 (1977) 1249–1256.
814   https://doi.org/10.1007/BF02643839.

815   [53]   A. López-Suárez, Influence of surface roughness on consecutively hydrogen
816   absorption cycles in Ti-6Al-4V alloy, Int. J. Hydrogen Energy. 35 (2010) 10404–
817   10411. https://doi.org/10.1016/j.ijhydene.2010.07.163.

818   [54]   J. Zhang, J. Li, Y. Han, Superhydrophobic PTFE Surfaces by Extension, Macromol.
819   Rapid Commun. 25 (2004) 1105–1108. https://doi.org/10.1002/marc.200400065.

820   [55]   Y.X. Ni, B. Feng, J. Wang, X. Lu, S. Qu, J. Weng, Decyl bis phosphonate-protein surface
821   modification of Ti-6Al-4V via a layer-by-layer technique, J. Mater. Sci. 44 (2009)
822   4031–4039. https://doi.org/10.1007/s10853-009-3562-0.

823

851   direct analysis of H2 bubbles. (b) OM images of H2 bubbles around the H-charging area. Left:

852   S4 specimen; Right: S2 specimen. (c) Amount of recombined H2 molecules per area by H-

853   charging time on the two specimens. (d) Percentages of H2 recombination (left y-axis) and H

854   ingress into specimen (right y-axis) in the total amount of electrochemical H reduction.

855   **Figure 8.** (a) H2 partial pressure-temperature curves of H-charged S2 and S4 specimens,

856   measured by TDS. (b-c) Deconvolution of each curve to individual Gaussian peaks - (b) S4

857   specimen, (c) S2 specimen.

858   **Figure 9.** SIMS ion maps for (a,b) S2 specimen and (c,d) S4 specimen. (a) and (c) shows

859   overlay of ion maps for Ti (TiO- signal, red) and Ni (NiO- signal, green). (b) and (d) show ion

860   maps of normalized H- signal. The schematic diagram between a and c describes the ramp

861   morphology, and the scale bar between (b) and (d) shows depth from the Ni/Ti-6Al-4V

862   interface in the ramp along the horizontal position in the H- signal maps. (e) Line profiles of

863   normalized H- signal along the horizontal arrow lines in (b) and (d).

864   **Figure 10.** Schematic illustration for surface roughness profiles with different skewness (*Sk*)

865   and kurtosis (*K*), in the cases of specimens S1 to S4. *Ra* and *m* is the arithmetic mean

866   roughness and mean height, respectively.

867   **Figure 11.** Representation of H behavior at polished flat surfaces and non-polished rough

868   surfaces with surface peaks. The rough surface is more active for recombination of Hads into

869   H2 due to the surface peaks and less H enters the material. The higher density of dislocations

870   under the rough surface also increases the amount of trapped H in the subsurface volume,

871   which blocks Habs diffusion further into the sample.

872

873

874 **List of tables**

875

876 **Table 1.** Details of the methods used to prepare the H-charging surface of each specimen.

877 Whole preparation steps of each specimen include the preparation steps of the one above it.

878 **Table 2.** Average mechanical properties of specimens obtained from three repeats for each

879 case.

880 **Table 3.** Surface area, averaged surface roughness parameters and height distribution

881 descriptor values obtained from the surface roughness maps in Figure 4.

882

Supplementary Materials

884

A. Error propagation analysis of the tensile test results of small specimens

In the main text, we focus our attention mostly on the difference in the failure strain between the non-polished (S1 and S2) and polished (S3 and S4) specimens. There are, however, as can be seen in Fig. 1 and Table 1, several other differences among the measured property values. To assess the significance of the differences, an error propagation analysis was carried out. Based on the measurement uncertainty of a digital micrometer (used to measure gauge thickness) and the estimated uncertainty in the optical microscope measurements (used to measure gauge width), the percentage uncertainty in the measurement of gauge area was calculated to be ~1%. This is four orders of magnitude higher than the percentage error in the force measurements from the micro-mechanical testing system, showing that the uncertainty in the stress is dominated by uncertainty in the area measurement. The respective uncertainties were combined through Equation (1) to generate a measured uncertainty (u_σ) in the proof stress and UTS measurements, where σ is the stress, A is the gauge area, and F is the force [34].

$$\left(\frac{u_\sigma}{\sigma}\right)^2 = \left(\frac{u_A}{A}\right)^2 + \left(\frac{u_F}{F}\right)^2 \tag{1}$$

From this analysis, the average error in both the proof stress and UTS values were calculated to be ~10 MPa. This error is not insignificant, but it is also not high enough to account entirely for the observed scatter generated from repeat measurements (as included in Table 2). The observed scatter ranges from 8-40 MPa in the proof stress and 7-27 MPa in the UTS based on three repeats. This discrepancy is likely a result of so-called 'scale effects', which influence variability when small test pieces are used [34]. Miniaturizing test coupons make experiments more susceptible to influence from factors such as residual stresses, misalignment and surface effects (particularly relevant here due to the different surface finishes used) [34]. This creates larger observed errors than those generated purely through measurement uncertainty, so it is these observed errors that the significance of the results will be measured against. In general, the variations in proof stress and UTS between

911 specimens fall within the range of the observed errors (based on repeats), so little attempt is
912 made to compare these values among specimens. An exception is the lower proof stress
913 exhibited by the polished specimens, which can be accepted as a feature of HE since the
914 magnitude by which they differ from the other specimens (~100 MPa) is significantly higher
915 than the observed scatter. Similarly, the differences in strain to failure between the S1, S2 and
916 uncharged specimens have not been directly compared, since their differences are
917 comparable to the observed scatter. However, the drastic decrease in fracture strain between
918 polished and non-polished specimens is certainly significant, since the change is several
919 times higher than the largest error reported. Therefore, we focus on the origin of the different
920 fracture strain in the H-charged specimens here – in other words, the different susceptibility
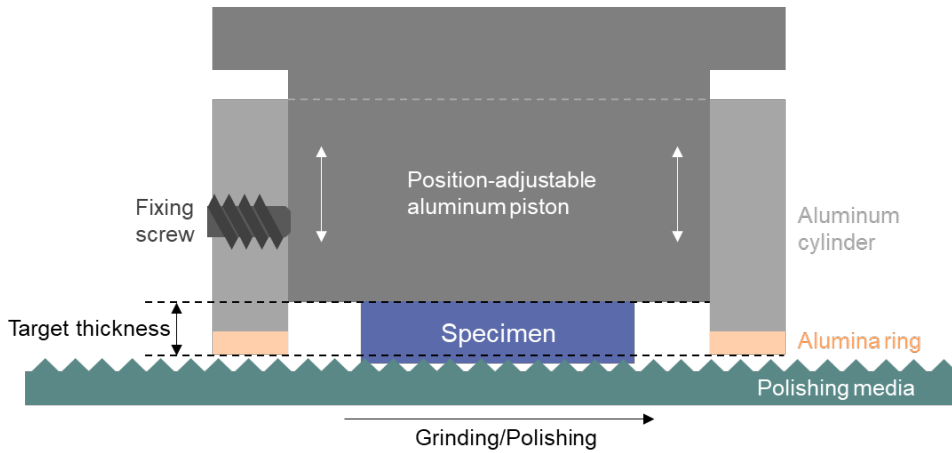921 to hydrogen embrittlement by surface state.

922

923 **B. Supplementary Figures**
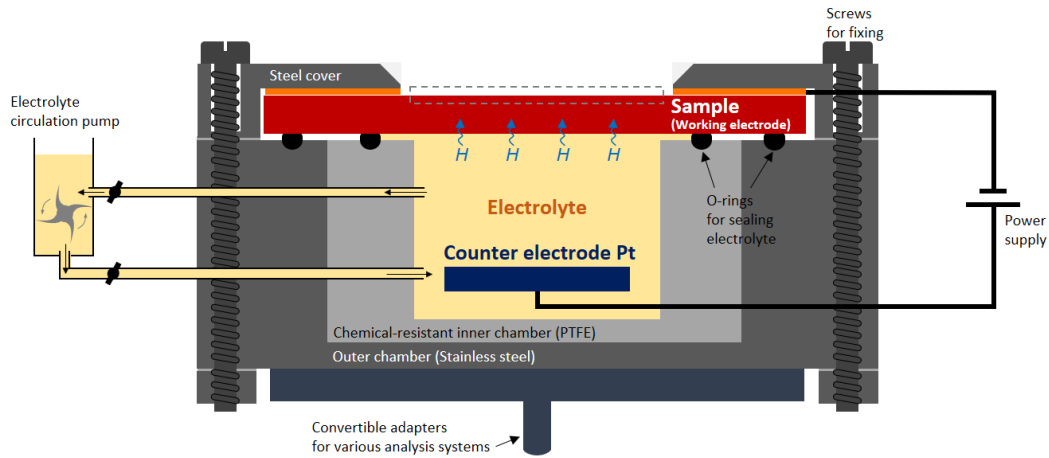
924
925 ***Figure SI1.*** *Schematic diagram of the electrochemical cell used in this study for H-charging (reproduced*
926 *from* [30]*).*
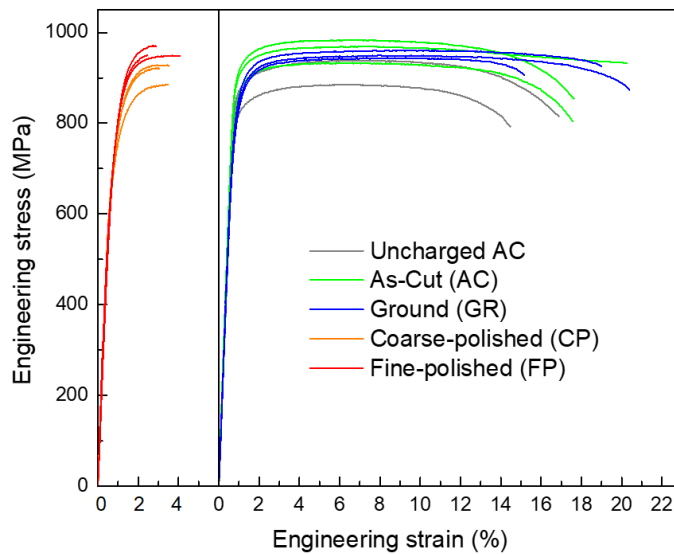
927

928

Figure SI2. *A thickness-controllable specimen mount used in specimen preparation in this study. The outer aluminum cylinder has an alumina ring with extremely low abrasion rate, which minimizes the thickness change of the outer body. A specimen can be glued on the position-adjustable piston, which enables to adjust the target thickness.*

933

934

Figure SI3. *Engineering stress-strain curves from all repeated tensile tests of specimens with different surface finishes after H-charging and uncharged S1 specimens.*

937
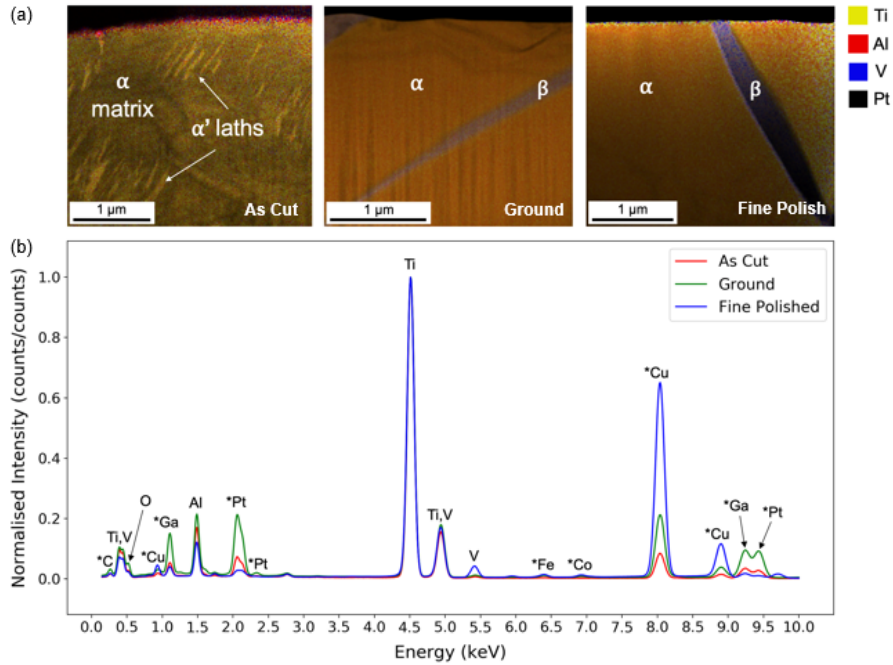
Figure SI4. *STEM-EDX results for As-Cut (S1), Ground (S2) and Fine Polish (S4) specimens. (a) Overlay maps showing the elemental distribution in the three specimens. (b) EDX spectra from the entire region in (a), with peaks labelled according to the elements that they represent. *Refers to elements not contained within the alloy; e.g. Cu from the EDM electrode wire and TEM sample holder.*
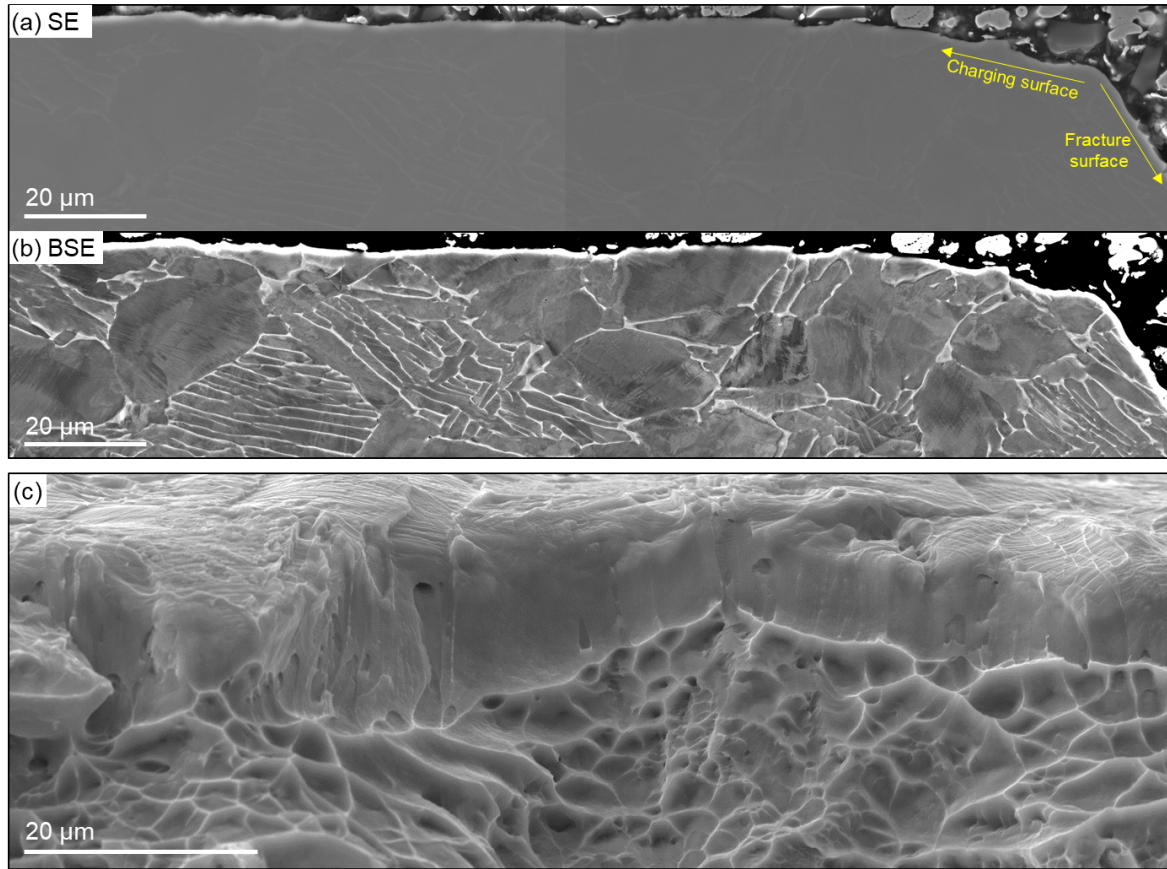

943
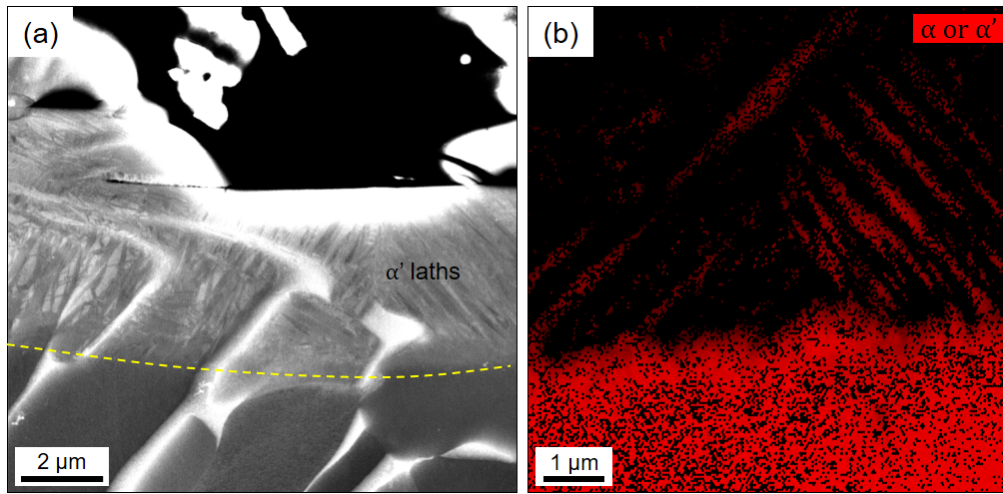
Figure SI5. *BSE micrograph of α' martensite region in the EDM white layer of the As-Cut (S1) specimen. (d) EBSD phase map of a region in the white layer, matching the laths to a hcp phase.*

Figure SI6. *(a,b) Cross-section SEM images of the H-charged S2 specimen after fracture; (a) SE and (b) BSE images. (c) SE image of the fracture surface of the H-charged S2 specimen near the charging surface.*